Effect of interplanetary magnetic field on hemispheric asymmetry in ionospheric horizontal and field-aligned currents during different seasons

A. B. Workayehu[1], H. Vanhamäki[1], A. T. Aikio[1], and S. G. Shepherd[2]

[1]Space Physics and Astronomy Research Unit, University of Oulu, Finland.
[2]Thayer School of Engineering, Dartmouth College, Hanover, NH, USA.

Key Points:

- Hemispheric asymmetry in auroral currents is larger for By^+ in NH (By^- in SH) than vice versa during both signs of IMF Bz
- Strongest asymmetry occurs in local winter and autumn for IMF By^+ in NH (By^- in SH) and IMF Bz^+ with NH/SH FAC ratio of about 1.18
- IMF By^+ in NH and By^- in SH causes larger auroral currents than vice versa. Effect is stronger for IMF Bz^+ than IMF Bz^-

Corresponding author: A. B. Workayehu, `abiyot.workayehu@oulu.fi`

Abstract

We present a statistical investigation of the effects of interplanetary magnetic field (IMF) on hemispheric asymmetry in auroral currents. Nearly six years of magnetic field measurements from Swarm A and C satellites are analyzed. Bootstrap resampling is used to remove the difference in the number of samples and IMF conditions between the local seasons and the hemispheres. Currents are stronger in Northern Hemisphere (NH) than Southern Hemisphere (SH) for IMF By^+ in NH (By^- in SH) in most local seasons under both signs of IMF Bz. For By^- in NH (By^+ in SH), the hemispheric difference in currents is small except in local winter when currents in NH are stronger than in SH. During By^+ and Bz^+ in NH (By^- and Bz^+ in SH), the largest hemispheric asymmetry occurs in local winter and autumn, when the NH/SH ratio of field aligned current (FAC) is 1.18±0.09 in winter and 1.17±0.09 in autumn. During By^+ and Bz^- in NH (By^- and Bz^- in SH), the largest asymmetry is observed in local autumn with NH/SH ratio of 1.16±0.07 for FAC. We also find an explicit By effect on auroral currents in a given hemisphere: on average By^+ in NH and By^- in SH causes larger currents than vice versa. The explicit By effect on divergence-free (DF) current during IMF Bz^+ is in very good agreement with the By effect on the cross polar cap potential (CPCP) from the Super Dual Auroral Radar Network (SuperDARN) dynamic model except at SH equinox and NH summer.

1 Introduction

The effect of the interplanetary magnetic field (IMF) on the magnetosphere-ionosphere current systems is well documented (e.g., Juusola et al., 2014; Reistad et al., 2014; Milan et al., 2017; Huang et al., 2017; Smith et al., 2017; Laundal et al., 2018, and references therein). The southward IMF Bz (IMF Bz^-) in the GSM (geocentric solar magnetospheric) reference frame causes an enhanced reconnection at the front of the magnetopause and allows a large amount of solar wind energy to enter into the Earth's magnetosphere, which subsequently increases the magnitudes of currents flowing in the coupled polar ionosphere. When the IMF Bz is northward (IMF Bz^+), reconnection occurs at a location behind the cusps when the IMF draped over the magnetopause merges with the already opened tail lobe field lines (e.g., Burke & Doyle, 1986; Russell, 2000, and references therein). During this time the amount of energy entering into the magnetosphere decreases and thus the intensity of currents in the polar ionosphere weaken. In addition to the IMF Bz, also the IMF Bx and By components and solar wind velocity have an effect on the auroral currents. The auroral current system consists of both the field aligned currents (FACs) and ionospheric horizontal currents. The horizontal part of the auroral current system can further be divided into Pedersen and Hall currents which can in many situations be approximated by the curl-free (CF) and divergence-free (DF) horizontal current components, respectively.

The auroral current systems are related to the electric field that is imposed on the ionosphere by the ionosphere-magnetosphere coupling as well as IMF polarity (e.g., Ruohoniemi & Greenwald, 2005; Haaland et al., 2007; Pettigrew et al., 2010; Cousins & Shepherd, 2010; Thomas & Shepherd, 2018, and references therein). In most of these studies, the IMF By component is seen to twist the average plasma convection patterns and electric field at the NH and SH to different direction, thereby creating hemispheric asymmetry. Ruohoniemi and Greenwald (2005) have studied factors that influence the convection of plasma in the northern hemisphere high-latitude ionosphere. They found greater cross polar cap potential for IMF By^+ than for By^- and more potential variation across the dusk cell than the dawn cell. Using vector measurements of the electron drift velocity by the Electron Drift Instrument (EDI) on Cluster, Haaland et al. (2007) found larger cross polar cap potential for IMF By^+ in the NH (By^- in the SH) than vice versa. Most recently, Thomas and Shepherd (2018) have found a linear increase in the cross polar cap potential with increasing Kp for a given IMF orientation at NH. Comparing By^+

and By^- for each Kp < 5, the CPCP is always larger for By^+ than for By^-. Pettigrew et al. (2010) have conducted a statistical study on the dipole tilt angle dependency and on the hemispheric symmetry of the high-latitude convection pattern and cross polar cap potential using Super Dual Auroral Radar Netwok (SuperDARN) measurements. Their results show that when the hemispheres are compared under opposite signs of IMF By during positive tilt (local summer) and neutral tilt (equinoxes), the cross polar cap potential of the hemisphere with IMF By^- is larger.

Previous studies have reported the effect of IMF By on the fluxes of high energy electron precipitation (e.g., Holappa et al., 2020) and substorm occurrence rates (e.g., Liou et al., 2020; Ohma et al., 2021, and references therein). Holappa et al. (2020) studied the explicit IMF By effect on the fluxes of high energy electron precipitation (>30 keV) in the auroral region. They found larger precipitation fluxes for IMF By^+ than IMF By^- in NH winter (SH summer), and vice versa in NH summer (SH winter). Liou et al. (2020) investigated the effect of IMF By polarity on the substorm occurrence rate and found about 33% more substorms for By^+ than for By^-. Recently, Ohma et al. (2021) reported a similar By effect on substorm activity, more specifically, they found that substorms occur more frequently when By and the dipole tilt angle have different signs as opposed to when they have the same sign.

Hemispheric asymmetry in auroral current systems has been reported in several previous studies (Green et al., 2009; Coxon et al., 2016; Laundal et al., 2016; Milan et al., 2017; Huang et al., 2017; Smith et al., 2017; Workayehu et al., 2019, 2020). Most of these studies reported larger average currents in the northern hemisphere (NH) than southern hemisphere (SH). In some studies the observed hemispheric difference was attributed to the satellite's orbital configuration (Green et al., 2009) or difference in the dayside reconnection (Coxon et al., 2016), while others raised data quality issues (Milan et al., 2017) and the role of data analysis methods (Laundal et al., 2017). Smith et al. (2017) have found a seasonal and IMF By sign dependent hemispheric asymmetry in the auroral electrojet. They found stronger (weaker) auroral electrojet currents in NH than in SH during By^+ (By^-) around the local winter. However, they did not find a significant IMF By effect on the auroral electrojet in the local summer season. Using Swarm magnetic field measurements Huang et al. (2017) found larger auroral electrojets in NH than in SH during local summer averaged over all IMF conditions. They also found that the prominent auroral electrojet currents are closely controlled by the solar wind energy input, but their intensity is not depend on IMF By orientation.

Very recently, Pakhotin et al. (2021), using Swarm A satellite data, studied electromagnetic energy input into the ionosphere by assessing the Poynting flux in the NH and SH. They found higher electromagnetic energy input into the NH than the SH even when averaged over season. They proposed that the observed hemispheric asymmetry in the electromagnetic energy input can be explained by the different solar illumination of the NH and SH auroral ovals.

Using Swarm A and C satellite data Workayehu et al. (2019), here after referred to as Paper I, examined hemispheric asymmetry in auroral currents during low (Kp $<$ 2) and high (Kp ≥ 2) geomagnetic activity conditions averaged over all local seasons. We found significant hemispheric asymmetry during low activity conditions, with about 10% more intense currents in NH than SH. Recently Workayehu et al. (2020), here after referred to as Paper II, studied the seasonal effect on FACs and horizontal currents using the same database as in Paper I with one extra year of data added. We found larger hemispheric asymmetry during low than high activity conditions, and during local winter and autumn seasons than during local spring and summer seasons, with more intense currents in NH than SH.

In this paper, we extend the analysis carried out in Papers I and II by studying the effect of IMF on the hemispheric asymmetry in the field aligned and ionospheric horizontal currents during different local seasons. Even though the main aim of the paper is to study the hemispheric asymmetry in the auroral currents, we also investigated the explicit By effect in a given hemisphere. We use Swarm data during the time period 15 April 2014 to 31 December 2019, which is about 8 months more than in Paper II. We utilize the Spherical Elementary Current Systems (SECS) data analysis method (Amm et al., 2015; Juusola et al., 2016; Vanhamäki et al., 2020) like in Papers I and II. To our knowledge this paper is the first systematic study of IMF effect on the hemispheric asymmetry in the full auroral current system (FAC, CF and DF current) during all seasons.

The rest of the paper is organized as follows: in Section 2, we briefly describe the data and data analysis methods including the bootstrap resampling method. In Section 3.1, we present the IMF dependence of FACs and ionospheric horizontal currents during different local seasons in NH and SH. In order to compare the hemispheric differences in the cross polar cap potential and associated electric field during different seasons, we calculate cross polar cap potential differences for different IMF orientations from the SuperDARN Dynamic Model (SDDM)(Cousins & Shepherd, 2010) in Section 4. Finally in Section 5, we present the summary and conclusions of the study.

2 Data analysis

2.1 Swarm data and SECS analysis method

The Swarm data set, magnetic field data analysis and coordinate systems used in the analysis were described in Paper I and II, and are briefly summarised here.

In this study, we utilize data measured by Swarm A and Swarm C satellites from 15 April 2014 to 31 December 2019. Specifically, we use the level-1b calibrated 1 Hz magnetic field data (the 0505 dataset). For FAC and horizontal current estimation, we first obtain the variation magnetic field data by subtracting a background magnetic field model from the measured magnetic field data. We use CHAOS-6-x8 model for April 15, 2014 - April 14, 2019 and CHAOS-7 for April 15 - December 31, 2019. CHAOS model is a geomagnetic field model combining Earth's core, crust and magnetospheric currents (Finlay et al., 2016).

The Spherical Elementary Current Systems (SECS) method (Amm et al., 2015; Juusola et al., 2016; Workayehu et al., 2019; Vanhamäki et al., 2020) is used to estimate FAC and horizontal currents. For estimating currents using the Swarm/SECS analysis method, we first discard magnetic data poleward of $\pm 80°$ geographic latitude, where the longitudinal separation between Swarm A and C becomes too small for a reliable current estimation using this method. Locations of the satellite's magnetic footpoints and the vector magnetic filed data are then converted to Spherical-AACGM (SPH-AACGM) coordinates (detailed description in Paper I).

The data from each orbit are divided into four overflights between $[\pm 50°, \pm 80°]$ SPH-AACGM latitudes, and we discard that part of an overflight where the satellite path is nearly parallel to the SPH-AACGM latitudes (gradient of latitude is $< 0.015°/\mathrm{s}$), since the analysis method fails in that situation. This condition is met more often in SH and most of the rejected points take place near $80°$ AACGM (Shepherd, 2014) latitude. Since we limit our analysis to SPH-AACGM latitudes lower than $80°$, NH is very little affected by this rejection procedure and even in SH the effect on currents flowing within the oval is negligible (see Paper II for detailed description).

2.2 IMF and solar wind data

In this study, we use the 1-min resolution interplanetary magnetic field and solar wind OMNI data propagated to the Earth's bow shock. We average the OMNI data over

30-min period before oval crossings and then use the average values to calculate Newell solar wind coupling function $d\Phi/dt$ (Newell et al., 2007).

To explore the effect of IMF on the hemispheric asymmetry in FACs and ionospheric horizontal currents during different local seasons, first we divide the oval crossings into four local seasons as we did in Paper II: NH spring and SH autumn (± 45 days around March equinox), NH summer and SH winter (± 45 days around June solstice), NH autumn and SH spring (± 45 days around September equinox), and NH winter and SH summer (± 45 days around December solstice). We further group the oval crossings in each local season into four IMF clock-angle sectors based on IMF By and Bz directions. Figure 1 shows the distribution of oval crossings as a function of values of the coupling function for the four local seasons and four clock-angle sectors in NH and SH. From now on we will denote the positive and negative directions for each IMF component with superscripts. For IMF Bz^+ conditions, the peak of the oval crossing distributions for all seasons is at the lowest bin, while for IMF Bz^- conditions the peak value locations are slightly different in the two hemispheres.

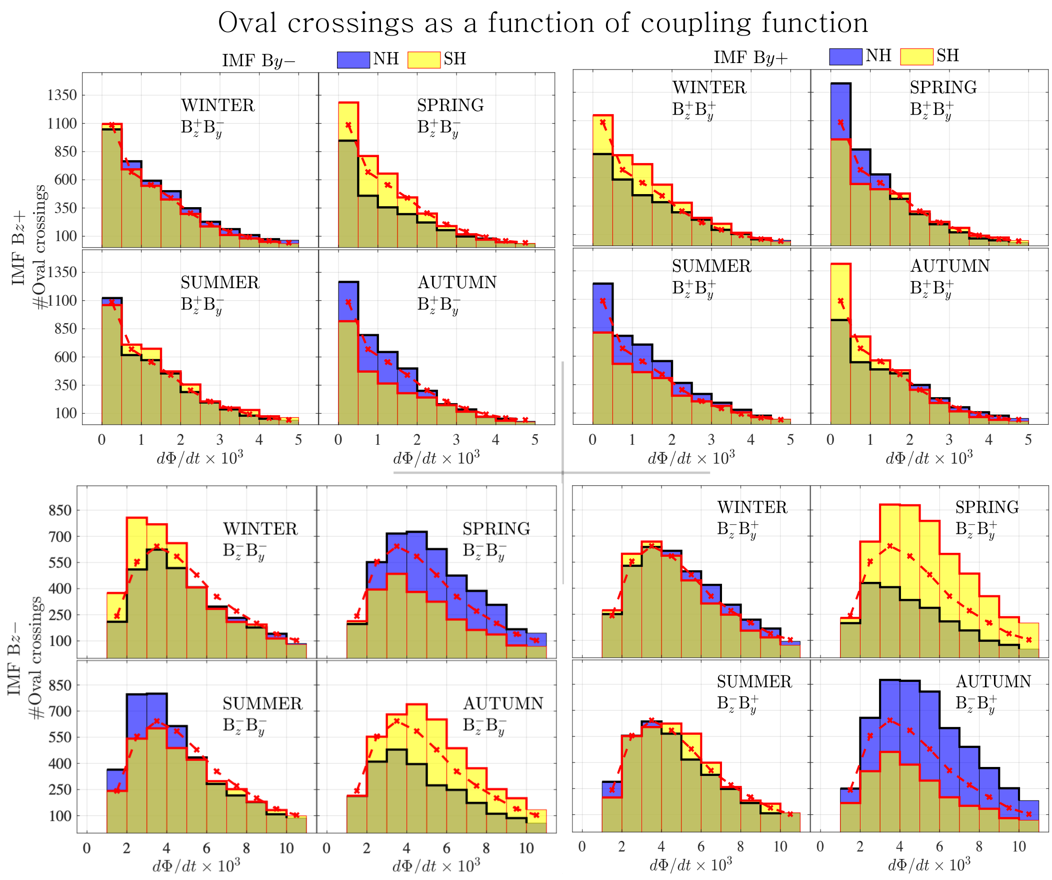

Figure 1. Distribution of Swarm oval crossings as function of Newell coupling function (dΦ/dt) for the four local seasons in the Northern (NH, blue) and Southern (SH, yellow) hemispheres. The distribution for each local season is sorted into four quadrants of IMF clock-angle: Bz^+By^-, B_z^+By^+, Bz^-By^+ and Bz^-By^-, where the superscripts denote the positive and negative directions of IMF Bz and By components. The red dashed line is the re-sampling (bootstrap) distribution of oval crossings. The blue and yellow distributions are for NH and SH, respectively.

2.3 Bootstrapping by using the Newell coupling function

From Figure 1, one can easily see the hemispheric differences in the coupling function distribution in each local season and IMF clock angle sectors. For example, in the Bz^-By^+ sector during local spring, the number of oval crossings in SH is larger than in NH, while the difference is vice versa during local autumn. Similarly, a relatively large hemispheric difference is also seen during local spring and autumn seasons in the Bz^-By^- sector.

We correct for the hemispheric and seasonal differences in the Newell coupling function distributions by using bootstrap resampling (also known as bootstrapping). Bootstrapping is a statistical method that relies on random sampling with replacement from the original data (e.g., Chernick & LaBudde, 2011; Dekking & Meester, 2005). In this study, the original data are the Swarm oval crossings in each local season and each IMF clock angle sector. In order to re-sample from the original data, we first define sampling distribution (or bootstrap distribution) according to which we randomly take samples from the original data distribution. The sampling distribution is defined in such a way that the total number of Swarm oval crossings in each coupling function bin is the same for the four seasons and the two hemispheres, separately for IMF Bz^+ and Bz^-. This way we get two sampling distributions, one for IMF Bz^+ conditions and another for IMF Bz^- conditions, which are used for all seasons and IMF By directions. These are shown by the red dashed lines in Figure 1. For each local season and clock-angle sector, a total of 1000 bootstrap samples are randomly taken with replacement from the original data. The numbers of oval crossings in each bootstrap sample are 3595 and 3571 for IMF Bz^+ and Bz^- conditions, respectively, which are the average number of oval crossings in the original data set per season for each direction of IMF Bz. A similar method was used in Paper II to make the local seasons directly comparable to each other in terms of Kp index, but in this study our aim is to make the local seasons and IMF By polarity under the same IMF Bz direction directly comparable to each other.

The average ionospheric horizontal currents and FACs in each 2° AACGM latitude by 1 h MLT grid cells are calculated for each of the 1000 bootstrap samples. The sizes of the grid cells in this paper are larger than the sizes of the grid cells in Papers I and II, as now we divide the data in each local season into four IMF quadrants. From the 1000 bootstrap samples, we have 1000 different distributions of the average values. The median values of the average current densities in each grid cell are then calculated from the bootstrap statistics. These results, presented in Section 3.1, are our best estimates for the current densities in each grid cell.

3 Results

3.1 Estimation of total currents

In Paper II, it was shown that the hemispheres are more asymmetric for low (Kp< 2) than high (Kp≥ 2) activity conditions, and in local winter and autumn when compared to local spring and summer seasons. Here we study how the IMF orientation affects the hemispheric asymmetry in auroral currents during different seasons.

In order to quantify the hemispheric differences in FACs and horizontal CF and DF currents, we calculate the total integrated FAC values, and the average horizontal CF and DF currents for the four IMF clock angle sectors during each local season and IMF direction using the same formula as in Papers I and II, summarized below.

The total integrated FAC flowing between [60°, 80°] AACGM latitudes and all MLTs is obtained by

$$\mathrm{I} = \sum_{m=1}^{M} |\mathrm{FAC}_m| \mathrm{S}_m, \tag{1}$$

where FAC_m is the FAC density in grid cell m, S_m is the physical grid cell area calculated by converting the AACGM grid cell (MLT versus AACGM latitude) to geographical coordinate system, and M is the total number of grid cells. The integrated FAC values contain contributions both from the upward and downward FACs.

For the CF and DF currents, we first calculate the magnitude of the current density in each grid cell as the square root of the sum of the squares of meridional (positive southward) and zonal (positive eastward) current density components. The average CF and DF current values between [60°, 80°] are then calculated between [60°, 80°] AACGM latitudes over all MLTs using the formula

$$I = \frac{1}{M} \sum_{m=1}^{M} \Delta_{m,\phi} \sqrt{J_{m,\phi}^2 + J_{m,\theta}^2}, \tag{2}$$

where $J_{m,\theta}$ and $J_{m,\phi}$ are the meridional and zonal current density components in grid cell m, respectively, M is the total number of grid cells between [60°, 80°] AACGM latitudes and over all MLTs, while $\Delta_{m,\phi}$ is the zonal dimension of the grid cell calculated by converting the AACGM grid cell (MLT versus AACGM latitude) to geographical coordinate system.

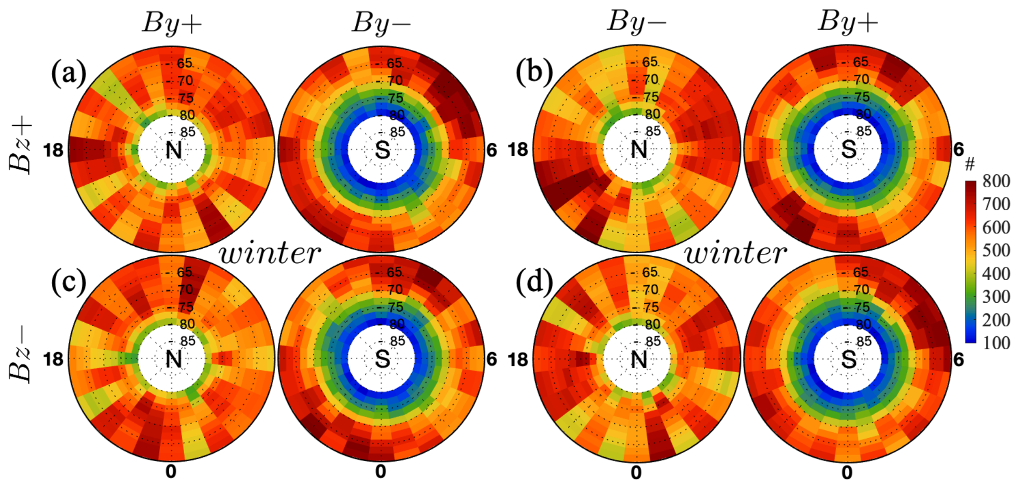

Figure 2. Bootstrapped data point distribution in local winter for the four IMF clock angle sectors in NH and SH. The plots are given in AACGM latitude by MLT. For both hemispheres, the noon (12 MLT) is at the top and evening (18 MLT) is at the left and the lowest latitude is 60°.

Figure 2 shows the bootstrapped distributions of data points in the two hemispheres for the local winter season. In each IMF Bz direction, the NH and SH have distributions for opposite IMF By next to each other. When we compare the hemispheres with each other in the subsequent sections, we select the IMF By direction in NH and use the opposite IMF By sign in SH. In all IMF sectors the NH has more data points than the SH poleward of ±66° AACGM latitude, while the SH has more samples between 60° and 65° AACGM latitudes. This is due to the difference in the locations of AACGM poles relative to the geographic poles in the two hemispheres and the Swarm A and C satellites' near polar orbits (see Figure 1 in Paper I). Other seasons (not shown here) have same kind of distributions.

3.2 IMF effect on current distributions in both hemispheres

In this section, we present the effect of IMF By direction on the magnitude and distributions of currents during each local season under northward and southward IMF Bz. In order to see the influence of IMF By on FACs, CF and DF currents during each local season more clearly, we calculate the ratios of the total integrated currents between the two IMF By directions for each hemisphere.

Figure 3 shows distributions of median FACs, CF and DF current densities obtained with bootstrapping in both hemispheres during local winter. As expected, stronger FACs (Figures 3a–3d) occur during IMF Bz^- than IMF Bz^+ for both hemispheres and IMF By signs (note the difference in color scales). Comparison of FACs during IMF B$y^{+/-}$ in each hemisphere separately indicates that the sign of By affects the magnitude and spatial distribution of FACs. in NH, FAC density during By^+ seems to be larger than during By^- conditions while in SH, FAC density during By^- seems to be larger than during By^+ conditions. In both hemispheres, strong median FACs occur in the premidnight MLT sector between 19–24 MLTs during all IMF clock angle sectors. This enhancement of FAC on the premidnight MLT sector during local winter season is in line with previous results reported by (e.g., Ohtani et al., 2005; Workayehu et al., 2020, and references)

Figure 3 shows also distributions of median CF (panels e - h) and median DF (panels i - l) current densities (both magnitude and vectors). In each hemisphere, the median CF and DF currents show generally similar IMF dependence as FACs: stronger median currents during IMF Bz^- than during IMF Bz^+ conditions, and during By^+ than By^- in NH (opposite IMF By sign in SH). A more closer comparison of median CF currents between the two IMF By signs in each hemisphere indicates that part of the CF current flowing from the dawnside to duskside across the polar cap occurs only when IMF By^+ in NH (By^- in SH) during both IMF Bz conditions. The eastward and westward flowing DF currents (see Figures 3i–3l) display the well-known eastward and westward electrojets, EEJ and WEJ, respectively. For all IMF sectors, the WEJ currents are stronger than the EEJ currents in both hemispheres. The WEJ current densities are stronger for IMF By^+ in NH (By^- in SH) than vice versa during both IMF Bz directions. Further more, the Harang discontinuity region, which is an overlap between EEJ and WEJ in the premidnight MLT sector with sharp latitudinal separation, occurs during all IMF sectors. This is in line with the result in Paper II, and here our result indicates that the IMF By sign doesn't affect the occurrence of Harang discontinuity during local winter.

Figure 4 shows distributions of the median current densities during local summer in the same format as Figure 3. Figures 4a–4d indicate that the post-noon and dusk (12-19 MLT) R1 FACs are stronger and flow in a wide range of MLTs when IMF By is negative in NH (Figures 4b and 4d) than when it is positive (Figures 4a and 4c). Conversely, the dawnside R1 FACs seem to be stronger when IMF By is positive in NH than vice versa. The median CF current distributions (Figures 4e–4h) show similar dawn/dusk imbalance with IMF By direction as the median FACs, but the effect of IMF By direction on the median DF current (Figures 4i–4l) seems smaller. However, a closer look to the WEJ indicates a tendency of stronger WEJ current for IMF By^- in NH (By^+ in SH) than vice versa. This is opposite to the IMF By on WEJ current during local winter.

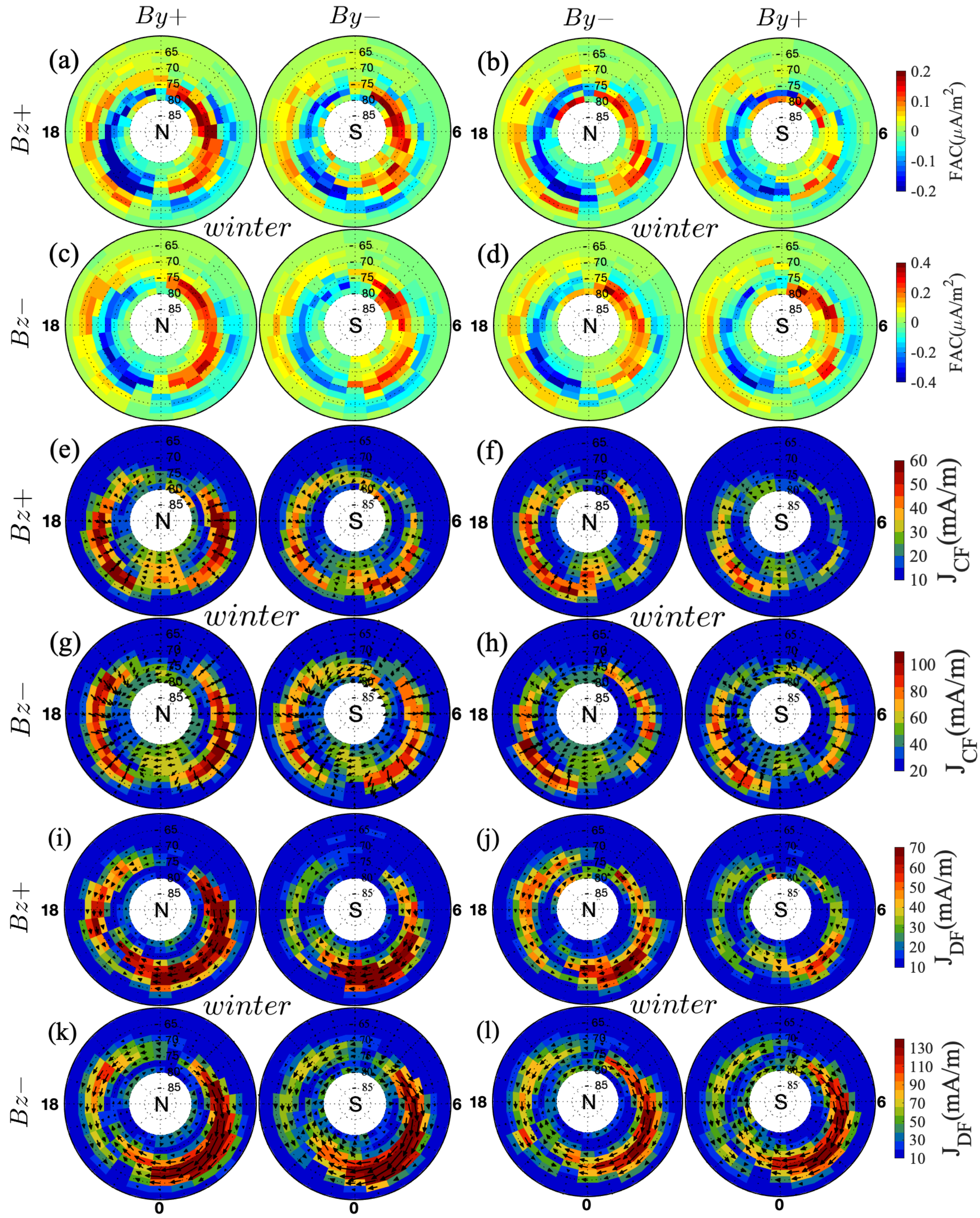

Figure 3. Distributions of median FAC density (a - d), median CF current density (e - h) and median DF current density (i - l) in local winter for the four IMF clock angles in NH and SH. Downward (upward) FACs are defined as positive (negative). The magnitudes and flow directions of median CF and DF currents are shown in color and arrows, respectively. From left to right: the first and second columns are for By^+ in NH and for By^- in SH, and the third and fourth columns are for By^- in NH and for By^+ in SH, respectively. From top to bottom: the first, third and fifth rows are for Bz^+, while the second, fourth and sixth rows are for Bz^-. The plots are given in AACGM latitude by MLT. For both hemispheres, the noon (12 MLT) is at the top and evening (18 MLT) is at the left and the lowest latitude is 60°. Note that the color scales for currents during IMF B_z^+ and B_z^- conditions are different.

Comparison of the AACGM latitude distributions of currents during local winter and summer in each hemisphere shows the well known winter-summer difference in the magnitudes of currents irrespective of the IMF directions. This effect is obviously associated with the winter-summer difference in the background ionospheric conductances due to solar illumination (see also Section 3 in Paper II). At the auroral oval and polar cap, solar induced ionospheric conductances are larger in local summer than in local winter, and due to this stronger CF currents flowing from dawn to dusk and return DF currents occur during local summer (see Laundal et al. (2016) for further discussion). When comparing current distributions in winter and summer at the premidnight MLT sector, there is the Harang discontinuity difference which we saw already in Paper II: The EEJ and WEJ are separated latitudinally during local winter and longitudinally during local summer.

Figures 5a–5l show distributions of currents in NH and SH for different IMF sectors during local spring. Like in local summer, the post-noon and dusk R1 FAC seems stronger and flows in a wide range of MLTs when By is negative in NH (Figures 5b and 5d) than when it is positive (Figures 5a and 5c) for IMF Bz^+. Distributions of median CF currents (Figures 5e–5h) show similar IMF By dependence as FACs. Unlike FACs and CF currents, distributions of DF currents (Figures 5i–5l) indicate that both EEJ and WEJ currents are stronger for IMF By^- in NH (By^+ in SH) than vice versa.

Figures 6a–6l show distributions of median FACs (Figures 6a–6d), median CF currents (Figures 6e–6h) and median DF currents (Figures 6i–6l) in NH and SH for different IMF sectors during local autumn. The FAC and CF current densities are stronger when By is positive in NH (negative in SH) than vice versa. Unlike for local spring, but like for local winter, both the EEJ and WEJ currents are larger for By^+ in NH (By^- in SH) than vice versa during both IMF Bz directions.

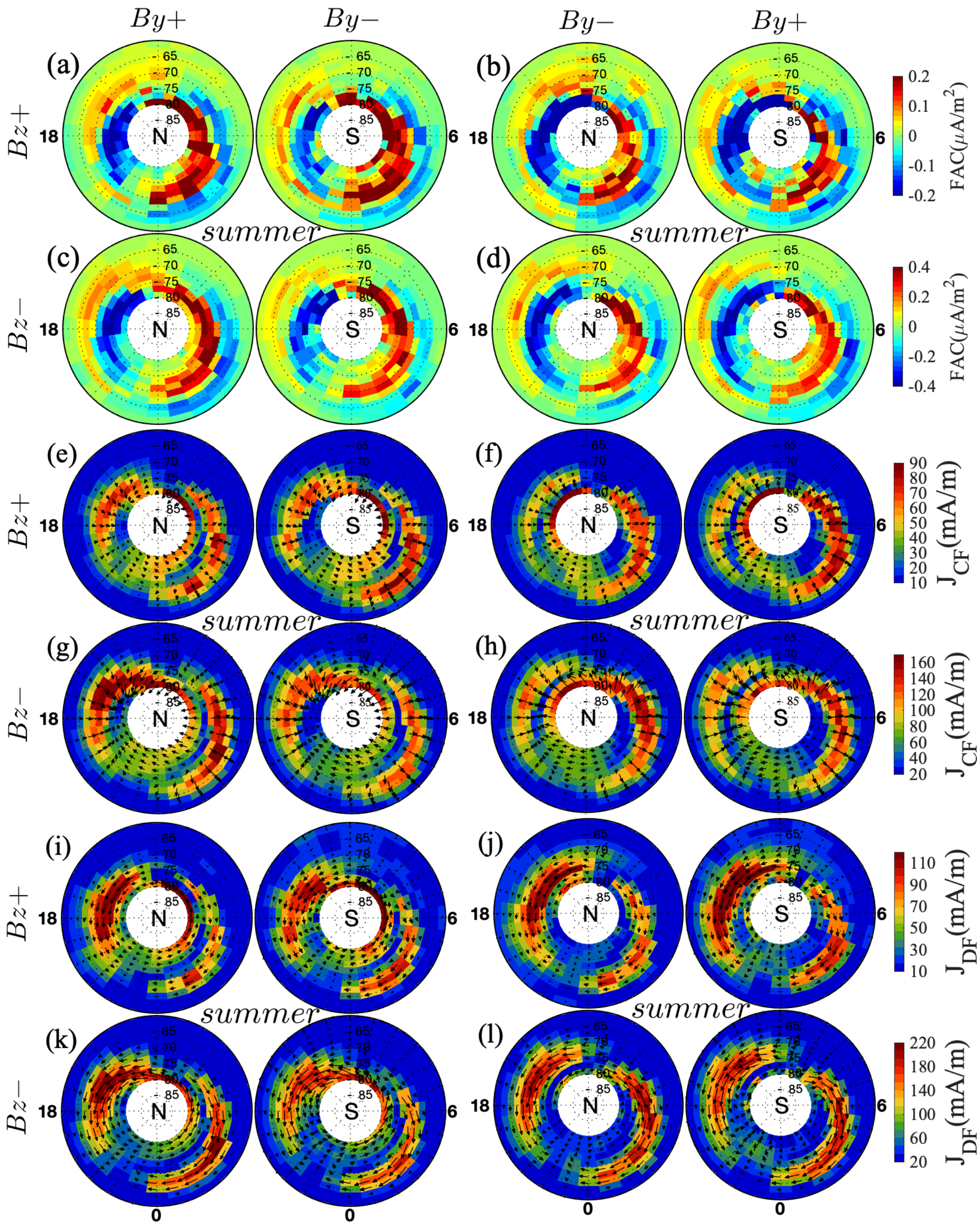

Figure 4. Same format as Figure 3, but for local summer.

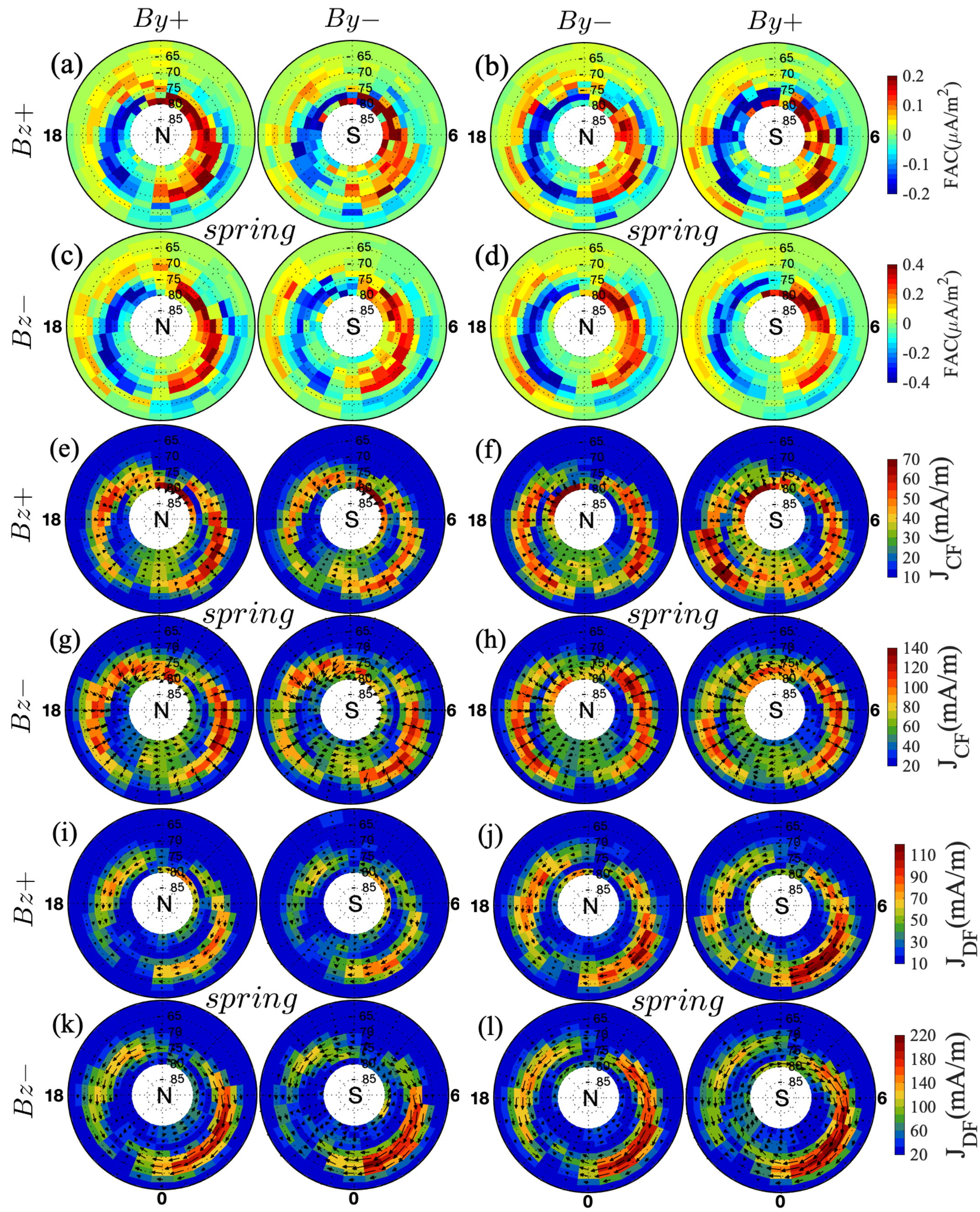

Figure 5. Same format as Figure 3, but for local spring.

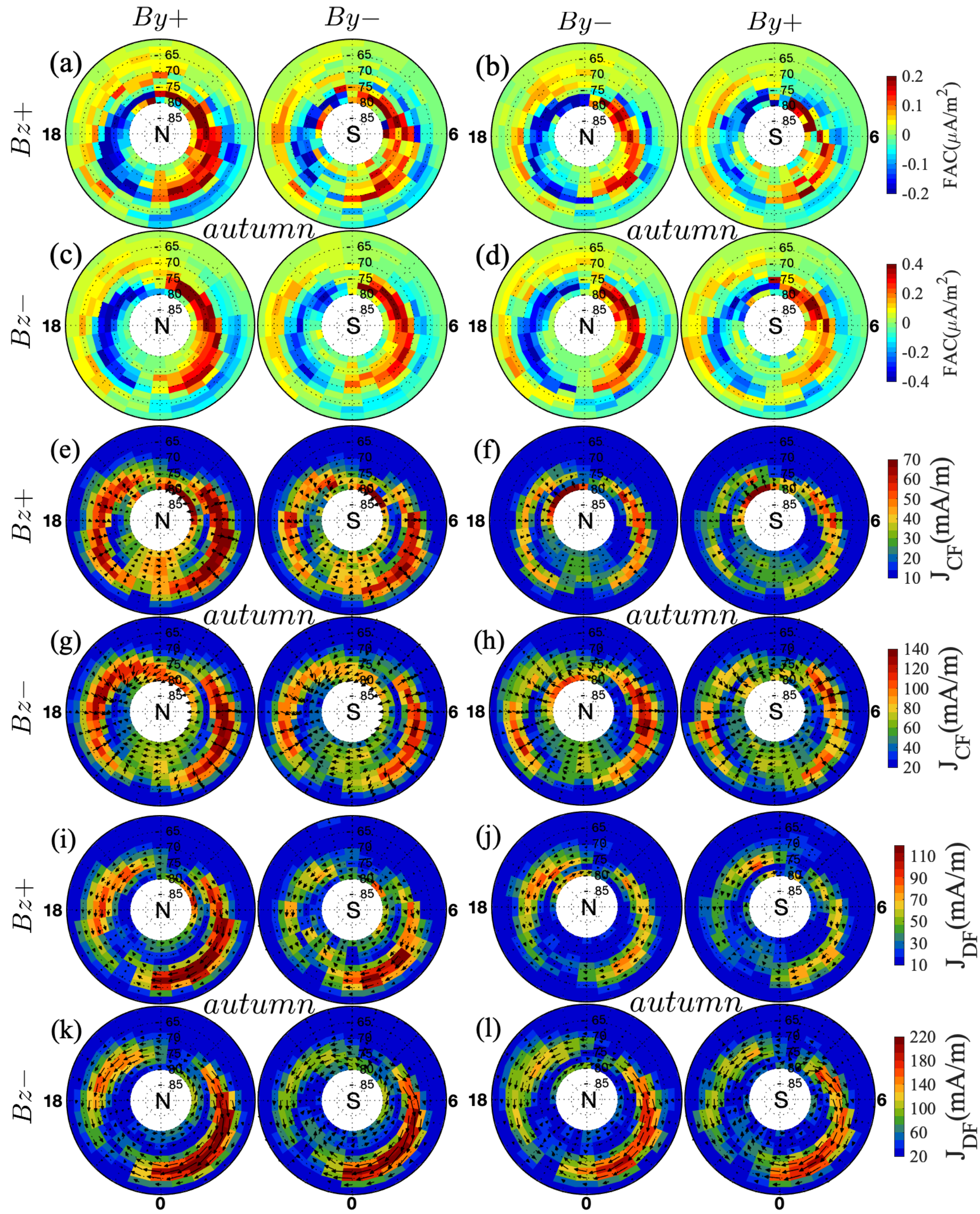

Figure 6. Same format as Figure 3, but for local autumn.

IMF	Currents	Winter	Spring	Autumn	Summer
(a) Integrated current ratios for opposite IMF By directions in NH: By^+/By^-					
Bz^+	FAC	1.21±0.09	0.98±0.07	1.36±0.09	1.01± 0.07
	I_{CF}	1.35±0.07	1.00±0.04	1.73±0.08	1.12±0.04
	I_{DF}	1.18±0.07	0.76±0.04	1.53±0.07	0.98±0.03
Bz^-	FAC	1.15±0.07	1.02±0.06	1.10±0.06	1.12±0.06
	I_{CF}	1.26±0.04	1.07±0.03	1.18±0.04	1.06±0.02
	I_{DF}	1.15±0.04	0.93±0.03	1.12±0.04	1.03±0.03
(b) Integrated current ratios for opposite IMF By directions in SH: By^-/By^+					
Bz^+	FAC	1.14±0.09	0.84±0.07	1.17±0.09	0.99±0.08
	I_{CF}	1.36±0.08	0.83±0.04	1.45±0.08	1.07±0.05
	I_{DF}	1.31±0.08	0.68±0.04	1.34±0.07	0.96±0.04
Bz^-	FAC	1.04±0.08	1.01±0.07	1.01±0.07	0.95±0.06
	I_{CF}	1.24±0.04	1.01±0.03	1.12±0.04	1.00±0.03
	I_{DF}	1.13±0.05	0.84±0.03	1.07±0.06	1.03±0.04

Table 1. Ratios of integrated currents for opposite IMF By directions in each hemisphere: By^+/By^- in NH (a) and By^-/By^+ in SH (b).

The results indicate that the IMF By has strong influence on auroral current systems in both hemispheres, but this influence depends on the local season and IMF Bz direction. In Table 1, we show ratios of currents for opposite IMF By directions in each hemisphere separately during both IMF Bz conditions. in NH (Table 1a) during IMF Bz^+ conditions, the largest IMF By effect on ionospheric currents occurs in local winter and autumn. In NH winter all the current components (FAC, CF and DF) are about 20-35% larger for IMF By^+ than By^-, while in autumn the effect is even larger, about 35-70%. In contrast, during NH spring and NH summer the effect is much smaller. Similar IMF By effect and seasonal pattern is visible also during IMF Bz^- conditions, but the effect is smaller, with the maximum enhancement of 15-20% during winter. Table 1b shows the IMF By effect in SH, but with the By signs switched. The seasonal and IMF Bz variations are similar to the NH, with the IMF By effect being larger during IMF Bz^+ and local winter and autumn. In contrast to NH, a large effect is also seen in local spring during IMF Bz^+ conditions, when the currents are 25-30% smaller for IMF By^- than for IMF By^+.

Overall, the IMF By effect tends to be stronger during IMF Bz^+ than IMF Bz^- conditions in both hemispheres. This is in line with Smith et al. (2017) results, even though they did not consider different seasons separately under different IMF conditions. Averaged over all seasons in NH, they found about 11% and 7% stronger auroral electrojet currents during IMF Bz^+ and IMF Bz^-, respectively, when IMF By is positive than when it is negative. However, they did not find a significant IMF By sign effect on the auroral electrojet current in SH during either IMF Bz direction, which is contrary to our finding.

3.3 IMF effect on hemispheric asymmetry in currents

Visual inspection of Figures 3–6 shows that IMF By affects the hemispheric asymmetry between NH and SH. In this section, we compare currents from the two hemispheres in terms of integrated current values and corresponding NH/SH ratios during each local season under opposite IMF By directions.

Figure 7 and Table 2a quantify the magnitudes of currents and NH/SH ratios during IMF Bz^+ in NH and SH under opposite IMF By directions. Figures 7a and 7b show the seasonal variations of integrated FACs when the sign of By in NH is positive and negative, respectively. The error bars are the 90% confidence ranges obtained from bootstrapping. For By^+ in NH (Figure 7a), hemispheric difference in FAC occurs in local winter and local autumn, when the integrated FAC is larger in NH than in SH. In contrast, during local spring and local summer the currents in the two hemispheres are equal within the confidence limits. In each hemisphere, comparison of the integrated FAC values during the equinoxes indicate a tendency of larger currents flowing during local autumn than spring spring, although in SH the effect is not statistically significant.

For By^- in NH (Figure 7b), the seasonal behavior is very different. The integrated FAC increases from local winter to spring and then decreases in local autumn and again reaches its peak value in local summer. Comparison of Figures 7a and 7b shows that IMF By has a strong effect on the seasonal variations of FAC during IMF Bz$^+$, especially during the equinoxes. In NH the integrated FAC is larger in autumn than in spring during By$^+$, and vice versa during By$^-$. In SH the By effect is opposite.

Figure 7c shows the seasonal variation of the median NH/SH ratios of FACs obtained from bootstrapping for opposite IMF By directions in the two hemispheres during IMF Bz^+. As these ratios are calculated for each bootstrap sample separately, the values in Figure 7c are not the ratios of the median values shown in Figures 7a and 7b, but in practice the difference is very small. For By^+ in NH (solid line, corresponds to Figure 7a), statistically significant asymmetry occurs in local winter and autumn with the NH/SH ratios 1.18±0.09 and 1.17±0.09, respectively (see Table 2a). For By^- in NH (dashed line, corresponding to Figure 7b), statistically significant hemispheric asymmetry occurs during local winter and spring, when the NH/SH ratios are 1.11±0.06 and 0.90±0.07, respectively.

Figures 7d–7e and Figures 7g–7h, quantify the seasonal variation of average CF and DF currents, respectively, during IMF Bz^+ conditions. For both IMF By signs, the seasonal pattern of average CF and DF currents are very similar to integrated FACs. For By^+ in NH (solid lines in Figures 7d and 7f), the largest hemispheric asymmetry occurs in local winter and local autumn, when the NH/SH ratios are 1.19±0.06 and 1.19±0.05 for CF currents, and 1.19±0.07 and 1.18±0.06 for DF currents (see Table 2a). Similarly, for By^- in NH (dashed lines), the largest asymmetry takes place in local winter, with NH/SH ratios of 1.20±0.07 for CF and 1.32±0.08 for DF currents (see Table 2a). In addition, statistically significant hemispheric asymmetry occurs in local spring and local summer, with larger currents flowing in SH than in NH. Like for FACs, CF and DF currents are larger in autumn than in spring for By$^+$ in the NH (By$^-$ in the SH) and vice versa for By$^-$ in the NH (By$^+$ in the SH).

The observed spring-autumn asymmetry in currents may be related to the spring-fall asymmetry in the amplitude of global geomagnetic activity reported in previous studies (e.g., Mursula et al., 2011, references therein). Mursula et al. (2011) found spring - fall asymmetry in geomagnetic activity, with maxima of Ap index alternating between spring and fall during the declining phases of two consecutive solar cycles, cycles 22 and 23. Our dataset is taken entirely from the declining phase of solar cycle 24, so it could be expected that the spring-autumn asymmetry in currents flips the other way in the next (or previous) solar cycle.

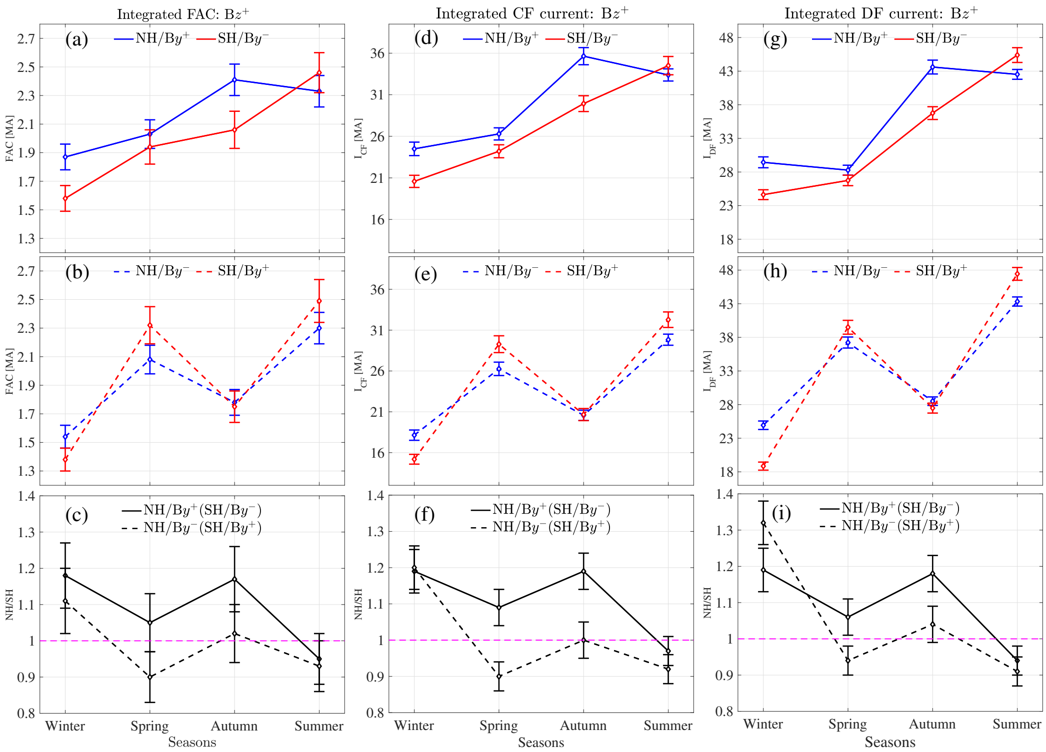

Figure 7. Median values of integrated FAC (panels: a-b, average CF (panels: d-e) and average DF (panels: g-h) currents as a function of season for IMF Bz^+ and opposite IMF By directions in NH and SH. The bottom panels are the median NH/SH ratios of FAC (c), CF current (f) and DF current (i). The error bars are the 90% confidence ranges.

Figure 8 and 2b show the integrated currents and hemispheric ratios for IMF Bz^- conditions, in the same format as Figure 7. When IMF By is positive in NH (Figure 8a), the smallest and largest integrated FAC occur in local winter and local summer, respectively, with the values in local spring and local autumn somewhere in between. Hemispheric difference occurs in local autumn and in local summer, with stronger currents flowing in NH than in SH. Similarly, when IMF By is negative in NH (Figure 8b), the smallest and largest integrated FAC occur in local winter and local summer, respectively. Unlike during IMF Bz^+ conditions shown in Figure 7b, the FAC values in local spring and local autumn are equal within the 90% confidence ranges in each hemisphere.

Figure 8c shows the seasonal variation of the median NH/SH ratios of FACs obtained from bootstrapping for opposite IMF By directions in the two hemispheres during IMF Bz^- conditions. When By is positive in NH (solid line), statistically significant hemispheric asymmetry in FAC occurs in local winter, autumn and summer, with NH/SH ratios (see Table 2b) 1.09 ± 0.07, 1.16 ± 0.07 and 1.11 ± 0.06, respectively. When By is negative in NH (dashed line), the two hemispheres are statistically symmetric during all local seasons, at the 90% confidence level.

Figures 8d–8f and 8g–8i show the seasonal variation of integrated CF and DF currents, respectively, in the same format as FAC. Overall, the seasonal variation patterns are very similar to each other and to the FAC. The largest hemispheric asymmetry in both CF and DF currents occur in local autumn for By^+ in NH (By^- in SH), when the NH/SH ratios are 1.15 ± 0.03 for CF current (see Figure 8f and Table 2b) and 1.13 ± 0.04 for DF current (see Figure 8g and Table 2b).

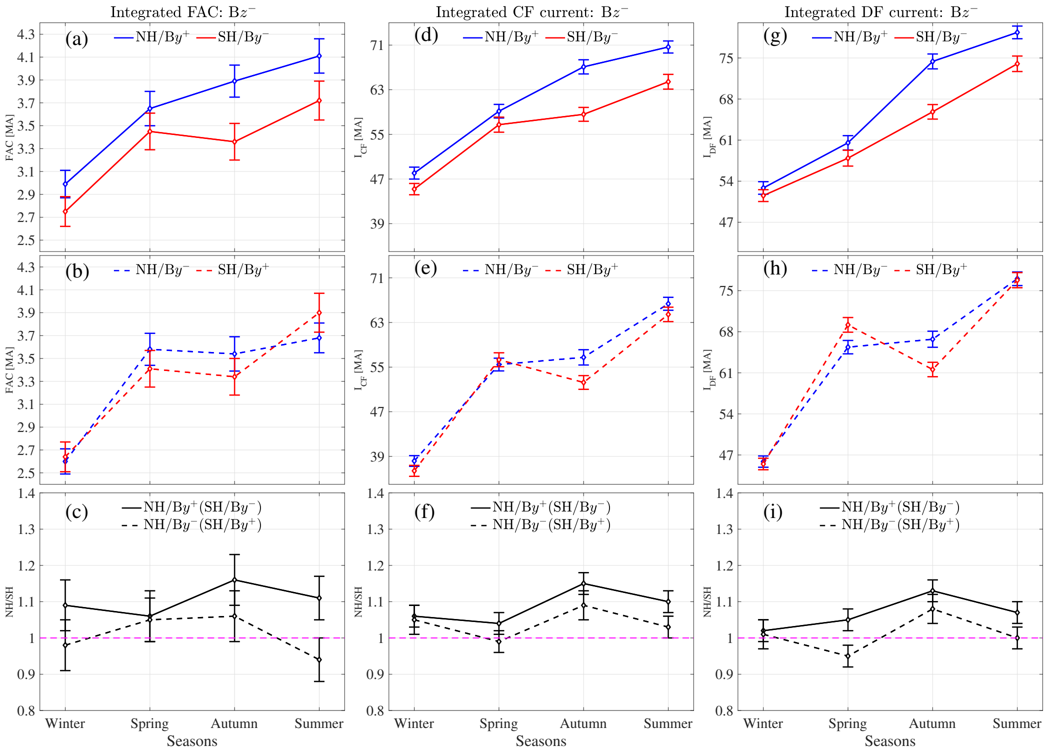

Figure 8. Same format as Figure 7, but for IMF Bz^-.

IMF By	Currents	Winter	Spring	Autumn	Summer
(a) NH/SH ratios of currents for opposite IMF By direction during IMF Bz^+					
By^+ NH (By^- SH)	FAC	1.18±0.09	1.05±0.08	1.17±0.09	0.95± 0.07
	I_{CF}	1.19±0.06	1.09±0.05	1.19±0.05	0.97±0.04
	I_{DF}	1.19±0.07	1.06±0.06	1.18±0.06	0.94±0.04
By^- NH (By^+ SH)	FAC	1.11±0.09	0.90±0.07	1.02±0.08	0.93±0.07
	I_{CF}	1.20±0.07	0.90±0.04	1.00±0.05	0.92±0.04
	I_{DF}	1.32±0.08	0.94±0.05	1.04±0.05	0.91±0.03
(b) NH/SH ratios of currents for opposite IMF By direction during IMF Bz^-					
By^+ NH (By^- SH)	FAC	1.11±0.09	0.90±0.07	1.02±0.08	0.93±0.07
	I_{CF}	1.06±0.04	1.04±0.04	1.15±0.03	1.10±0.03
	I_{DF}	1.02±0.04	1.05±0.04	1.13±0.04	1.07±0.03
By^- NH (By^+ SH)	FAC	0.98±0.07	1.05±0.07	1.06±0.07	0.94±0.06
	I_{CF}	1.05±0.04	0.99±0.03	1.09±0.04	1.03±0.03
	I_{DF}	1.01±0.04	0.95±0.03	1.08±0.04	1.00±0.03

Table 2. NH/SH ratios of integrated currents for opposite IMF By directions: during IMF Bz^+ (a, same as in Figure 7) and during IMF Bz^- (b, same as in Figure 8). For both IMF Bz conditions, the values in the first and second rows are for By^+ in NH (By^- in SH) and for By^- in NH (By^+ in SH), respectively.

Overall, the difference in hemispheric current intensities is smaller during IMF Bz^- (Figures 8c,f,i) than during IMF Bz^+ (Figures 7c,f,i). This is consistent with Paper II, where it was found that the hemispheric asymmetry is larger during low than high Kp conditions. Moreover, in each hemisphere, the IMF By effect on the integrated currents is larger during IMF Bz^+ (Figure 7) than during IMF Bz^- (Figure 8).

4 Cross polar cap potential from SuperDARN Dynamic Model

The FACs and ionospheric horizontal currents are closely related to the electric field imposed on the ionosphere by the ionosphere-magnetosphere coupling. In Paper II, we have speculated that an external forcing related to hemispherically asymmetric convection electric field and/or particle precipitation may play a role on the hemispheric asymmetry in the auroral current systems.

The ionospheric convection electric field is commonly expressed in terms of the cross polar cap potential difference (CPCP) or patterns of plasma convection velocity (e.g., Juusola et al., 2014; Cousins & Shepherd, 2010; Pettigrew et al., 2010; Thomas & Shepherd, 2018). The cross polar cap potential have been calculated from measurements by satellites and ground based radars such as the Super Dual Auroral Radar Network (SuperDARN). Several statistical models of high latitude plasma convection have been developed using SuperDARN radar data (e.g., Ruohoniemi & Greenwald, 1996, 2005; Pettigrew et al., 2010; Cousins & Shepherd, 2010; Thomas & Shepherd, 2018).

In this study, the SuperDARN Dynamical Model (SDDM) of high latitude plasma convection is used to calculate the cross polar cap potential difference and the plasma drift velocity for different seasons and IMF clock angle sectors. SDDM is based on Cousins and Shepherd (2010) convection model coefficients, hereafter called the CS10 model, which is an expansion of the convection model by Pettigrew et al. (2010). The CS10 convection model is based on 8 years of measurements from 9 northern and 6 southern hemisphere SuperDARN radars. Recently, several radars were added to the northern hemisphere SuperDARN offering improved coverage at mid-latitudes and in the polar cap region (Thomas & Shepherd, 2018). However, the radar coverage in the southern hemisphere has not significantly changed since the CS10 model. Thus the SDDM is the best tool for hemispheric comparison of the convection, as the difference between the hemispheres in the number of radars used for this model was not as large as it is now.

In addition to the relative sparsity of radar coverage in the SH, the radar fields-of-view in both hemispheres are concentrated towards the polar cap region (see Figure 1 in Pettigrew et al. (2010)). This configuration is not ideal during strong IMF Bz^-, as the oval and convection cells expand equatorward and may not be covered by SH radars. Because of this situation, we calculate the CPCP values for each local season only during IMF Bz^+ for both signs of IMF By in NH and SH. In the SDDM the seasonal effects are parameterize by dipole tilt angle values. We use $+15°$ dipole tilt for summer, -15° for winter and 0° for equinoxes (spring and autumn). As input to the SDDM, we take the values of IMF Bz^+ and solar wind velocity from their corresponding bootstrapped distributions, namely +2.0 nT for Bz and 400 km/s for the velocity. We repeat the calculation for IMF By values in the range [-6, 6] nT with 1 nT steps. During each local season, the NH/SH ratios of CPCP are calculated for equal magnitudes but opposite IMF By signs between the two hemispheres. Standard deviations are calculated for each IMF By sign separately using the six values in the range [±1, ±6] nT.

Figures 9a and 9b, respectively, show the CPCP as a function of IMF By in NH and in SH for different local seasons during IMF Bz^+. In both hemispheres, the CPCP values increase as the magnitude of IMF By increases. However, there is a clear difference in the seasonal CPCP pattern as a function of By in each hemisphere. In NH, the local seasons are more similar to each other for IMF By^+ (solid lines) than for IMF By^- (dashed lines), while the opposite is true in SH. For IMF By^- in NH and IMF By^+ in SH, the CPCP values on average are largest in local summer, intermediate in equinox

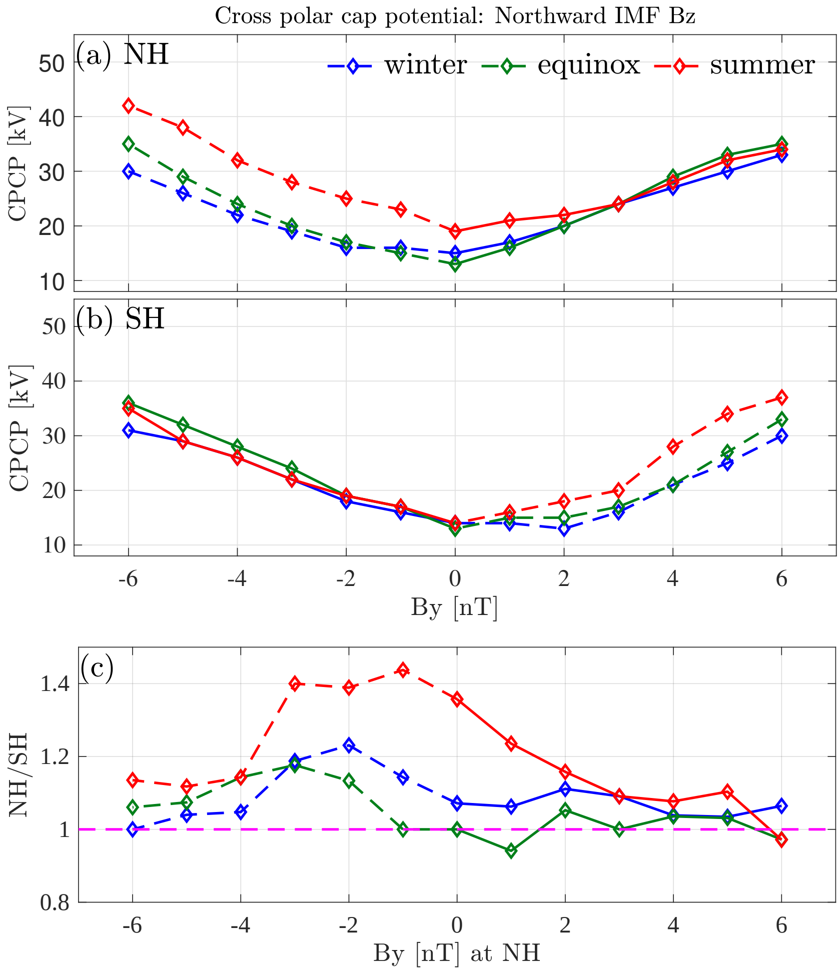

Figure 9. Cross polar cap potential difference as a function of IMF By in NH (a) and in SH (b) during IMF Bz^+ for different local seasons. Panel (c) shows the NH/SH ratios of CPCP for opposite signs of IMF By: solid and dashed lines are for IMF By^+ and for IMF By^- in NH, respectively. The horizontal axis shows the values of IMF By in NH.

and smallest in local winter. Larger CPCP in local summer than in local winter was reported also in previous studies (e.g., Ruohoniemi & Greenwald, 2005; Pettigrew et al., 2010).

Figure 9c shows the NH/SH ratios of CPCP for opposite IMF By plotted as a function of IMF By values in NH. Dashed and solid lines are NH/SH ratios of dashed and solid lines from Figures 9a and 9b. The ratios indicate that the CPCP values are larger in NH than in SH. Overall, the hemispheric difference is larger for IMF By^- in NH (By^+ in SH) than vice versa.

Figures 10a and 10b, respectively, show the NH/SH ratios of CPCP and DF current for opposite IMF By as a function of seasons. As the SDDM uses the dipole tilt angle to represent seasonal variations, the CPCP in local autumn and local spring are always equal. In Figure 10a the CPCP ratios in each local season are obtained by averaging the ratios shown in Figure 9c over all values of IMF By for each sign separately. During local winter, the NH/SH ratio of CPCP is larger than 1 for both signs of IMF By in NH, which is in agreement with the NH/SH ratio of DF current, but the CPCP

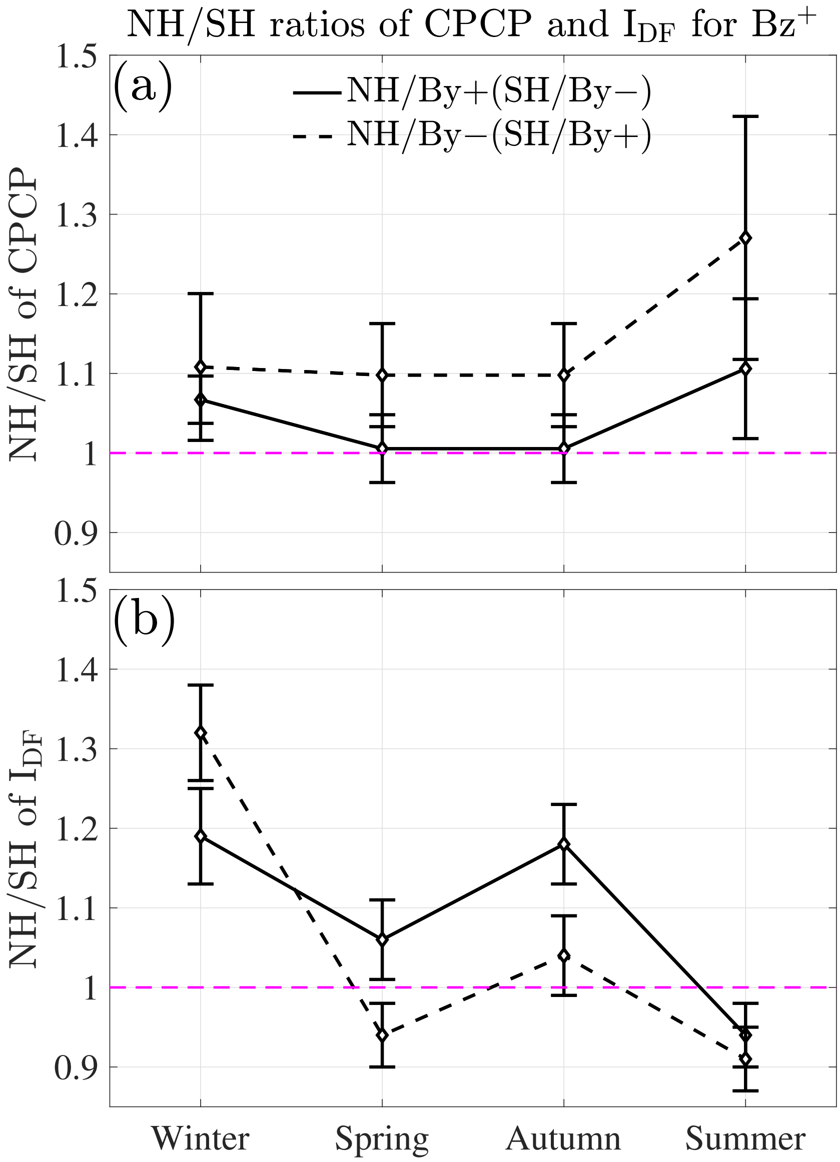

Figure 10. (a) NH/SH ratios of CPCP averaged over all IMF By^+ in NH (solid line) or IMF By^- in NH (dashed line) as a function of season. The error bars are standard deviations showing the variability of CPCP due to variability in the IMF By values. (b) median NH/SH ratios of DF current (same as Figure 7i).

NH/SH ratios are smaller than the DF NH/SH ratios. However, unlike the DF current, the largest hemispheric difference in CPCP occurs in local summer for IMF By^- in NH. For all local seasons, the average NH/SH ratios of CPCP are larger for IMF By^- in NH than vice versa. In contrast, for most seasons, larger hemispheric asymmetry in the DF current occurs for IMF By^+ in NH than vice versa. In fact, in Figure 10a the dashed line is always above the solid line and vice versa in Figure 10b (except in winter).

Next we move to discuss the explicit By effect in a given hemisphere for CPCP values. Table 3 shows the CPCP ratios for By^+/By^- in the NH and By^-/By^+ in the SH during both IMF Bz conditions. In both hemispheres, the largest By effect on CPCP occurs in local winter and equinox during IMF Bz^+ conditions, when the CPCP values are 13-24% larger for IMF By^+ in NH and IMF By^- in SH than vice versa. In NH summer, CPCP value is larger for By^- than vice versa, while in SH summer the By effect is not statistically significant. Similar IMF By effect is visible also during IMF Bz^- conditions, but the effect is smaller, with the maximum enhancement of 8% in SH equinox.

CPCP ratios for opposite IMF By directions: By^+/By^- in NH, By^-/By^+ in SH

IMF	Hemisphere	Winter	Equinox	Summer
Bz^+	NH	1.18±0.08	1.13±0.08	0.86± 0.04
	SH	1.22±0.14	1.24±0.12	0.99±0.09
Bz^-	NH	1.05±0.02	0.98±0.03	0.89±0.05
	SH	1.02±0.04	1.08±0.06	0.99±0.06

Table 3. Ratios of CPCP for opposite IMF By directions in each hemisphere: By^+/By^- in NH and By^-/By^+ in SH.

Figure 11 presents the ratios of CPCP (same as Table 3) and DF current (data from Table 1) for opposite IMF By in each hemisphere. Here, we compare the effect of By on CPCP with DF current, which can be assumed to represent the auroral electrojets. As the SDDM uses the dipole tilt angle to represent seasonal variations, the CPCP in local autumn and local spring are always equal. Therefore we have combined the DF current statistics from spring and autumn. During IMF Bz^+, the explicit By effect on CPCP and DF current is similar in winter and equinox for NH (Figure 11a), and in winter and summer for SH (Figure 11b). During IMF Bz^-, in NH the seasonal behaviour is rather similar both for CPCP and DF (Figure 11c), but in SH the pattern is not very clear (Figure 11d). Altogether, the ratios for Bz^- are smaller than for Bz^+. Largest differences occur during equinoxes in SH for both signs of Bz, but we should keep in mind that the SDDM doesn't make a difference between spring and autumn. In both hemispheres, the maximum By effect on both CPCP and DF current occurs in local winter during IMF Bz^+ conditions, when both the CPCP and DF current By^+/By^- ratios are about 1.18 in NH and By^-/By^+ ratios are about 1.20–1.30 in SH. Overall, the results indicate that the effect of By on DF current is in very good agreement with the SuperDARN dynamic model CPCP during IMF Bz^+ in winter for both hemispheres, at equinox for NH and in summer for SH.

When using the CPCP values and comparing them to the DF current as shown in Figures 10 and 11, one should keep in mind that there are some uncertainties and limitations in the SDDM model. As discussed before, the radar coverage in the SH is more limited than in the NH. Furthermore, the amount of data used to derive the CS10 coefficient can be rather limited for extreme values of the dipole tilt angle and large solar wind driving conditions. However, in our case the largest solar wind electric field used as input to the SDDM model is 2.5 mV/m, so our model values do not correspond to any extreme conditions and statistics are sufficient (see Figure 2 in Cousins and Shepherd (2010)).

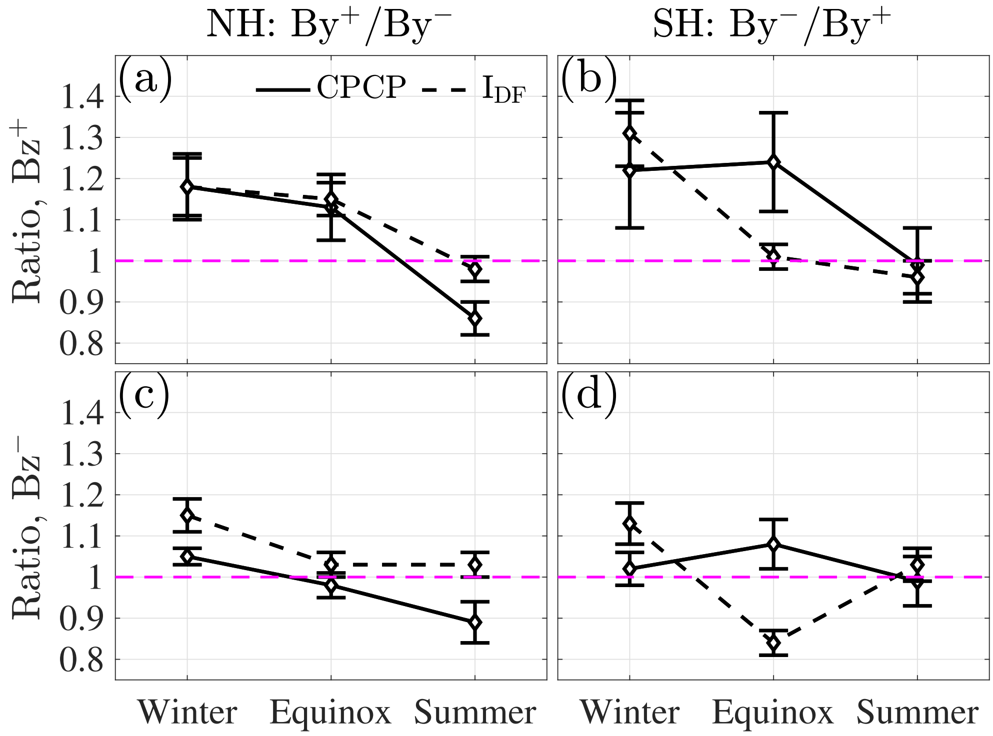

Figure 11. Ratios of CPCP (solid line) and DF current (dashed line) for opposite IMF By directions in NH (a, c) and in SH (b, d) during IMF Bz^+ (a, b) and Bz^- (c, d) conditions.

5 Summary and conclusions

In this paper, we have investigated the effect of the IMF on the hemispheric asymmetry in auroral currents measured by the Swarm satellites. The SECS method is used to estimate the FAC as well as the CF and DF parts of the ionospheric horizontal currents from nearly six years of Swarm vector magnetic field measurements. The data is divided into seasons and four IMF sectors based on the signs of the IMF Bz and By. In order to make the seasons and IMF By sectors comparable, bootstrap resampling technique is used to remove hemispheric and seasonal bias in the number of samples and in the Newell universal coupling function distributions.

We calculate the integrated FAC and average CF and DF currents for different seasons and IMF sectors, and the corresponding NH/SH ratios. The two hemispheres are compared under opposite IMF By signs. We also study the effect of the IMF By sign in a given hemisphere. Finally, in order to study the role of electric field in the hemispheric asymmetry of the auroral currents, we calculate the CPCP values using the SuperDARN dynamic model for both signs of IMF By during IMF Bz^+ only, because the coverage of the radars in the SH does not extend to as low latitudes as in the NH, which is likely important for IMF Bz^- conditions.

The most important findings of this paper are the following:

- The hemispheric asymmetry in auroral currents is larger during Bz^+ (northward) than Bz^- (southward) IMF conditions in local winter, irrespective of the IMF By sign. This is in line with previous result in Paper II, where we observed the strongest asymmetry in local winter during low Kp conditions.

- For By^+ in NH (By^- in SH), on average FACs as well as ionospheric horizontal currents are stronger in NH than in SH in most local seasons under both signs of IMF Bz. For IMF By^- in NH (By^+ in SH), the hemispheric differences of auroral currents are small except in local winter.
- During Bz^+ and By^+ in NH (Bz^+ and By^- in SH), hemispheric asymmetry in auroral currents is largest in local winter and local autumn, and smallest in local summer. The NH/SH ratio for FACs in winter and autumn are 1.18±0.09 and 1.17±0.09, respectively.
- During Bz^- and By^+ in NH (Bz^- and By^- in SH), hemispheric asymmetry in auroral currents is largest in local autumn for these IMF conditions. The NH/SH ratio for FAC, CF current and DF current in local autumn are 1.16±0.07, 1.15±0.03 and 1.13±0.03, respectively.
- Generally, in NH By^+ causes larger horizontal currents and FACs than By^-. The effect is stronger for Bz^+ (northward) than Bz^- (southward) IMF. For Bz^+, the By effect is statistically significant in Autumn (strongest) and Winter, for Bz^- in Autumn (strongest), Winter and Summer (weakest). The effect is not seen in the NH Spring. SH has a corresponding behavior for reversed By signs, but the effect is weaker in the SH, so generally it is seen only in Autumn and Winter.
- The explicit By effect in a given hemisphere for currents can tentatively be explained by the SuperDARN dynamic model CPCP for IMF Bz^+ in winter for both hemispheres, at equinox for NH and in summer for SH. Hence, in winter both the DF current and CPCP By^+/By^- ratios are about 1.18 in NH and By^-/By^+ ratios are about 1.2–1.3 in SH.
- However, when the hemispheric asymmetry is studied using the SuperDARN dynamic model, the CPCP NH/SH ratios for IMF Bz^+ do not, in general, agree with the behavior of auroral current ratios. Only in winter, both the CPCP and auroral currents show NH/SH ratios over 1 for both signs of IMF By. Furthermore, during IMF Bz^+ the highest NH/SH value of 1.27 in CPCP is obtained for summer, while for auroral currents the value is below 1.0 during summer.

In addition to the convective electric field, the magnitude of currents in the auroral ionosphere depends on auroral conductance due to particle precipitation. In Paper II, we studied the role of background conductances, but the role of precipitation could not be investigated with IRI. Using Swarm A magnetic and electric field measurements, Ivarsen et al. (2020) investigated the relationship between precipitation induced conductance and Alfvén wave reflection. They found a larger Alfvén wave reflection coefficient in the NH than in the SH, which they interpreted as a consequence of hemispheric asymmetry in the precipitation induced conductance, with the largest hemispheric asymmetry seen during local winter. This is in line with the hemispheric asymmetry in the auroral currents observed in this study as well as in Paper II. Therefore, the occurrence of stronger auroral currents in the NH than in the SH during local winter might be explained by a hemispherically asymmetric particle precipitation.

Regarding the explicit By effect in a given hemisphere, our results are in agreement with several other previous studies (e.g., Smith et al., 2017; Laundal et al., 2018, references therein). Using data from observations of different satellites, Smith et al. (2017) found larger auroral electrojet current in the NH winter for IMF By^+ and in the SH winter for IMF By^- than vice versa. Using Average Magnetic field and Polar current System (AMPS) model, Laundal et al. (2018) investigated the ionospheric horizontal and field-aligned currents in the NH polar region for different seasons and orientations of the IMF. They reported larger total FAC and DF current for IMF By^+ than for IMF By^- during both IMF Bz conditions in winter. This is in line with our result (see Table 1) that the FAC, CF and DF current in NH winter and spring are larger for IMF By^+ than for IMF By^-. Our results also show similar IMF By dependence of FAC, CF and DF currents in the SH, but for opposite polarity of IMF By.

The factors causing the observed hemispheric asymmetries in the auroral currents require still further investigations. The CPCP values from the SuperDARN dynamic model shown in this paper suggest that the convection electric field can not fully explain the hemispheric asymmetry in auroral currents. In Paper II, we have concluded that local background conductances from IRI model cannot explain the hemispheric asymmetry in auroral currents as the IRI model does not reproduce auroral zone conductivities due to particle precipitation. The effect of auroral precipitation induced conductivities for the hemispheric asymmetry during different IMF conditions and different seasons should be studied by using measurements and modeling.

Acknowledgments

This work was supported by the Academy of Finland (project 314664) and National Science Foundation (grant: AGS-1934997). The European Space Agency (ESA) is acknowledged for providing the Swarm data. The calibrated 1 Hz Swarm magnetic field data are available at `ftp://swarm-diss.eo.esa.int`. The OMNI data were obtained from NASA/GSFC's Space Physics Data Facility's OMNIWeb at `http://omniweb.gsfc.nasa.gov`. The CHAOS model (CHAOS-6-x8 and CHAOS-7) is available at `http://www.spacecenter.dk/files/magnetic-models/CHAOS-6`. The SuperDARN dynamic model is available at `http://sdnet.thayer.dartmouth.edu/models/dynamicmodel.php#SDDM`. SuperDARN is a collection of radars funded by national scientific funding agencies of Australia, Canada, China, France, Italy, Japan, Norway, South Africa, United Kingdom and the United States of America. The Altitude adjusted corrected geomagnetic (AACGM) coordinate transformation software is available at `http://superdarn.thayer.dartmouth.edu/aacgm.html`. The authors greatly appreciate the availability of the software from these websites.

References

Amm, O., Vanhamäki, H., Kauristie, K., Stolle, C., Christiansen, F., Haagmans, R., … Escoubet, C. P. (2015). A method to derive maps of ionospheric conductances, currents, and convection from the Swarm multisatellite mission. *Journal of Geophysical Research: Space Physics*, *120*(4), 3263–3282. Retrieved from `http://dx.doi.org/10.1002/2014JA020154` (2014JA020154) doi: 10.1002/2014JA020154

Burke, W. J., & Doyle, M. A. (1986). Interplanetary control of high latitude electrodynamics. *Journal of geomagnetism and geoelectricity*, *38*(11), 1115-1141. doi: 10.5636/jgg.38.1115

Chernick, M. R., & LaBudde, R. A. (2011). *An introduction to Bootstrap methods with applications to R.* Thomas Jefferson University, US: John Wiley Sons, Inc.

Cousins, E. D. P., & Shepherd, S. G. (2010). A dynamical model of high-latitude convection derived from SuperDARN plasma drift measurements. *Journal of Geophysical Research: Space Physics*, *115*(A12). Retrieved from `https://agupubs.onlinelibrary.wiley.com/doi/abs/10.1029/2010JA016017` doi: 10.1029/2010JA016017

Coxon, J. C., Milan, S. E., Carter, J. A., Clausen, L. B. N., Anderson, B. J., & Korth, H. (2016). Seasonal and diurnal variations in AMPERE observations of the birkeland currents compared to modeled results. *Journal of Geophysical Research: Space Physics*, *121*(5), 4027–4040. Retrieved from `http://dx.doi.org/10.1002/2015JA022050` (2015JA022050) doi: 10.1002/2015JA022050

Dekking, C. L. H., F.M. Kraaikamp, & Meester, L. (2005). *A modern introduction to probability and statistics.* Springer-Verlag London: Springer-Verlag London.

Finlay, C. C., Olsen, N., Kotsiaros, S., Gillet, N., & Tøffner-Clausen, L. (2016, Jul 11). Recent geomagnetic secular variation from Swarm and ground observatories as estimated in the CHAOS-6 geomagnetic field model. *Earth, Planets and Space*, *68*(1), 112. Retrieved from https://doi.org/10.1186/s40623-016-0486-1 doi: 10.1186/s40623-016-0486-1

Green, D. L., Waters, C. L., Anderson, B. J., & Korth, H. (2009). Seasonal and interplanetary magnetic field dependence of the field-aligned currents for both Northern and Southern Hemispheres. *Annales Geophysicae*, *27*(4), 1701–1715. Retrieved from https://www.ann-geophys.net/27/1701/2009/ doi: 10.5194/angeo-27-1701-2009

Haaland, S. E., Paschmann, G., Förster, M., Quinn, J. M., Torbert, R. B., McIlwain, C. E., ... Kletzing, C. A. (2007). High-latitude plasma convection from cluster EDI measurements: method and IMF-dependence. *Annales Geophysicae*, *25*(1), 239–253. Retrieved from https://www.ann-geophys.net/25/239/2007/ doi: 10.5194/angeo-25-239-2007

Holappa, L., Asikainen, T., & Mursula, K. (2020). Explicit imf dependence in geomagnetic activity: Modulation of precipitating electrons. *Geophysical Research Letters*, *47*(4), e2019GL086676. Retrieved from https://agupubs.onlinelibrary.wiley.com/doi/abs/10.1029/2019GL086676 (e2019GL086676 10.1029/2019GL086676) doi: 10.1029/2019GL086676

Huang, T., Lühr, H., & Wang, H. (2017). Global characteristics of auroral Hall currents derived from the Swarm constellation: dependences on season and IMF orientation. *Annales Geophysicae*, *35*(6), 1249–1268. Retrieved from https://www.ann-geophys.net/35/1249/2017/ doi: 10.5194/angeo-35-1249-2017

Ivarsen, M. F., Park, J., Kwak, Y.-S., Jin, Y., Knudsen, D. J., & Clausen, L. B. N. (2020). Observational evidence for the role of hall conductance in alfvén wave reflection. *Journal of Geophysical Research: Space Physics*, *125*(12), e2020JA028119. Retrieved from https://agupubs.onlinelibrary.wiley.com/doi/abs/10.1029/2020JA028119 (e2020JA028119 10.1029/2020JA028119) doi: https://doi.org/10.1029/2020JA028119

Juusola, L., E.Milan, S., Lester, M., Grocott, A., & M. Imber, S. (2014). Interplanetary magnetic field control of the ionospheric field-aligned current and convection distributions. *Journal of Geophysical Research: Space Physics*, *119*(4), 3130–3149. Retrieved from http://dx.doi.org/10.1002/2013JA019455 doi: 10.1002/2013JA019455

Juusola, L., Kauristie, K., Vanhamäki, H., Aikio, A., & van de Kamp, M. (2016). Comparison of auroral ionospheric and field-aligned currents derived from Swarm and ground magnetic field measurements. *Journal of Geophysical Research: Space Physics*, *121*(9), 9256–9283. Retrieved from http://dx.doi.org/10.1002/2016JA022961 (2016JA022961) doi: 10.1002/2016JA022961

Laundal, K. M., Cnossen, I., Milan, S. E., Haaland, S. E., Coxon, J., Pedatella, N. M., ... Reistad, J. P. (2017, Mar 01). North-South asymmetries in Earth's magnetic field. *Space Science Reviews*, *206*(1), 225–257. Retrieved from https://doi.org/10.1007/s11214-016-0273-0 doi: 10.1007/s11214-016-0273-0

Laundal, K. M., Finlay, C. C., & Olsen, N. (2016, Aug 11). Sunlight effects on the 3D polar current system determined from low Earth orbit measurements. *Earth, Planets and Space*, *68*(1), 142. Retrieved from https://doi.org/10.1186/s40623-016-0518-x doi: 10.1186/s40623-016-0518-x

Laundal, K. M., Finlay, C. C., Olsen, N., & Reistad, J. P. (2018). Solar wind and seasonal influence on ionospheric currents from Swarm and CHAMP measurements. *Journal of Geophysical Research: Space Physics*, *123*(5), 4402-4429. Retrieved from https://agupubs.onlinelibrary.wiley.com/doi/abs/10.1029/2018JA025387 doi: 10.1029/2018JA025387

Liou, K., Sotirelis, T., & Mitchell, E. (2020). Control of the east-west component of the interplanetary magnetic field on the occurrence of magnetic substorms. *Geophysical Research Letters*, *47*(5), e2020GL087406. Retrieved from https://agupubs.onlinelibrary.wiley.com/doi/abs/10.1029/2020GL087406 (e2020GL087406 2020GL087406) doi: https://doi.org/10.1029/2020GL087406

Milan, S. E., Clausen, L. B. N., Coxon, J. C., Carter, J. A., Walach, M.-T., Laundal, K., … Anderson, B. J. (2017, Mar 01). Overview of solar wind–magnetosphere–ionosphere–atmosphere coupling and the generation of magnetospheric currents. *Space Science Reviews*, *206*(1), 547–573. Retrieved from https://doi.org/10.1007/s11214-017-0333-0 doi: 10.1007/s11214-017-0333-0

Mursula, K., Tanskanen, E., & Love, J. J. (2011). Spring-fall asymmetry of substorm strength, geomagnetic activity and solar wind: Implications for semiannual variation and solar hemispheric asymmetry. *Geophysical Research Letters*, *38*(6). Retrieved from https://agupubs.onlinelibrary.wiley.com/doi/abs/10.1029/2011GL046751 doi: 10.1029/2011GL046751

Newell, P. T., Sotirelis, T., Liou, K., Meng, C.-I., & Rich, F. J. (2007). A nearly universal solar wind-magnetosphere coupling function inferred from 10 magnetospheric state variables. *Journal of Geophysical Research: Space Physics*, *112*(A1). Retrieved from https://agupubs.onlinelibrary.wiley.com/doi/abs/10.1029/2006JA012015 doi: 10.1029/2006JA012015

Ohma, A., Reistad, J. P., & Hatch, S. M. (2021). Modulation of magnetospheric substorm frequency: Dipole tilt and imf by effects. *Journal of Geophysical Research: Space Physics*, *126*(3), e2020JA028856. Retrieved from https://agupubs.onlinelibrary.wiley.com/doi/abs/10.1029/2020JA028856 (e2020JA028856 2020JA028856) doi: https://doi.org/10.1029/2020JA028856

Ohtani, S., Ueno, G., & Higuchi, T. (2005). Comparison of large-scale field-aligned currents under sunlit and dark ionospheric conditions. *Journal of Geophysical Research: Space Physics*, *110*(A9). Retrieved from https://agupubs.onlinelibrary.wiley.com/doi/abs/10.1029/2005JA011057 doi: 10.1029/2005JA011057

Pakhotin, I. P., Mann, I. R., Xie, K., Burchill, J. K., & Knudsen, D. J. (2021). Northern preference for terrestrial electromagnetic energy input from space weather. *Nature Communications*, *12*(1), 199. doi: 10.1038/s41467-020-20450-3

Pettigrew, E. D., Shepherd, S. G., & Ruohoniemi, J. M. (2010). Climatological patterns of high-latitude convection in the northern and southern hemispheres: Dipole tilt dependencies and interhemispheric comparisons. *Journal of Geophysical Research: Space Physics*, *115*(A7). Retrieved from https://agupubs.onlinelibrary.wiley.com/doi/abs/10.1029/2009JA014956 doi: 10.1029/2009JA014956

Reistad, J. P., Østgaard, N., Laundal, K. M., Haaland, S., Tenfjord, P., Snekvik, K., … Milan, S. E. (2014). Intensity asymmetries in the dusk sector of the poleward auroral oval due to IMF Bx. *Journal of Geophysical Research: Space Physics*, *119*(12), 9497-9507. Retrieved from https://agupubs.onlinelibrary.wiley.com/doi/abs/10.1002/2014JA020216 doi: 10.1002/2014JA020216

Ruohoniemi, J. M., & Greenwald, R. A. (1996). Statistical patterns of high-latitude convection obtained from goose bay hf radar observations. *Journal of Geophysical Research: Space Physics*, *101*(A10), 21743-21763. Retrieved from https://agupubs.onlinelibrary.wiley.com/doi/abs/10.1029/96JA01584 doi: 10.1029/96JA01584

Ruohoniemi, J. M., & Greenwald, R. A. (2005). Dependencies of high-latitude plasma convection: Consideration of interplanetary magnetic field, seasonal, and universal time factors in statistical patterns. *Journal of Geophysical Research: Space Physics*, *110*(A9). Retrieved from https://

agupubs.onlinelibrary.wiley.com/doi/abs/10.1029/2004JA010815 doi: 10.1029/2004JA010815

Russell, C. T. (2000). The solar wind interaction with the earth's magnetosphere: a tutorial. *IEEE Transactions on Plasma Science*, *28*(6), 1818-1830. doi: 10.1109/27.902211

Shepherd, S. G. (2014). Altitude-adjusted corrected geomagnetic coordinates: Definition and functional approximations. *Journal of Geophysical Research: Space Physics*, *119*(9), 7501–7521. Retrieved from http://dx.doi.org/10.1002/2014JA020264 doi: 10.1002/2014JA020264

Smith, A. R. A., Beggan, C. D., Macmillan, S., & Whaler, K. A. (2017). Climatology of the auroral electrojets derived from the along-track gradient of magnetic field intensity measured by pogo, magsat, champ, and swarm. *Space Weather*, *15*(10), 1257-1269. Retrieved from https://agupubs.onlinelibrary.wiley.com/doi/abs/10.1002/2017SW001675 doi: 10.1002/2017SW001675

Thomas, E. G., & Shepherd, S. G. (2018). Statistical patterns of ionospheric convection derived from mid-latitude, high-latitude, and polar superdarn hf radar observations. *Journal of Geophysical Research: Space Physics*, *123*(4), 3196-3216. Retrieved from https://agupubs.onlinelibrary.wiley.com/doi/abs/10.1002/2018JA025280 doi: 10.1002/2018JA025280

Vanhamäki, H., Juusola, L., Kauristie, K., Workayehu, A., & Käki, S. (2020). Spherical elementary current systems applied to swarm data. In M. W. Dunlop & H. Lühr (Eds.), *Ionospheric multi-spacecraft analysis tools: Approaches for deriving ionospheric parameters* (pp. 35–53). Cham: Springer International Publishing. Retrieved from https://doi.org/10.1007/978-3-030-26732-2_3 doi: 10.1007/978-3-030-26732-2_3

Workayehu, A. B., Vanhamäki, H., & Aikio, A. T. (2019). Field-aligned and horizontal currents in the northern and southern hemispheres from the swarm satellite. *Journal of Geophysical Research: Space Physics*, *124*(0). Retrieved from https://agupubs.onlinelibrary.wiley.com/doi/abs/10.1029/2019JA026835 doi: 10.1029/2019JA026835

Workayehu, A. B., Vanhamäki, H., & Aikio, A. T. (2020). Seasonal effect on hemispheric asymmetry in ionospheric horizontal and field-aligned currents. *Journal of Geophysical Research: Space Physics*, *125*(10), e2020JA028051. Retrieved from https://agupubs.onlinelibrary.wiley.com/doi/abs/10.1029/2020JA028051 (e2020JA028051 10.1029/2020JA028051) doi: 10.1029/2020JA028051